https://doi.org/10.5194/egusphere-2026-2836
Preprint. Discussion started: 16 June 2026
© Author(s) 2026. CC BY 4.0 License.

High-resolution glacier mapping reveals inventory biases and terrain controls on debris-covered glaciers in the Karakoram

Xin Yang[1,2], Shiyin Liu[1,2,3,*], Fuming Xie[4], Jinyue Wei[1,2], Jun Zhou[1,2], Yunpeng Duan[1,2], Yiyuan Shen[1,2], Yu Zhu[5], Qiao Liu[6], Muhammad Mannan Afzal[1,2], Muhammad Saifullah[7]

[1]Yunnan Provincial Key Laboratory of International Rivers and Transboundary Eco-security, Kunming 650500, China

[2]Institute of International Rivers and Eco-security, Yunnan University, Kunming, China

[3]Yunnan International Joint Laboratory of China-Laos-Bangladesh-Myanmar Natural Resources Remote Sensing Monitoring, Kunming 650500, China

[4]School of Earth Science, Yunnan University, Kunming, China

[5]College of Geography and Environmental Science, Northwest Normal University, Lanzhou 730070, China

[6]Institute of Mountain Hazards and Environment, Chinese Academy of Sciences, Chengdu 610041, China

[7]Department of Agricultural Engineering, Muhammad Nawaz Shareef University of Agriculture, Multan, Pakistan

Correspondence: Shiyin Liu (shiyin.liu@ynu.edu.cn)

Abstract: Accurate glacier inventories are fundamental for quantifying glacier change, estimating ice volume and assessing meltwater resources. However, medium-resolution inventories often fail to resolve critical glacier characteristics in topographically complex and debris-rich mountain environments. Here, we present the 2 m Karakoram Glacier Inventory (2mKGI), developed from high-resolution ZiYuan-3 (ZY-3) optical imagery, a co-registered ZY-3 digital elevation model (DEM) and auxiliary optical datasets through an integrated deep-learning and manual-refinement framework. The inventory identifies ~13,900 glaciers covering 21,261.8 ± 278 km², including 2,239.9 ± 82.8 km² of supraglacial debris, with an overall mapping uncertainty of ±4.7%. Comparison with existing inventories reveals that previous medium-resolution products commonly underestimate glacier numbers while simultaneously overgeneralizing debris-covered glacier margins. These biases substantially influence glacier-count statistics, estimates of debris-covered area, and the interpretations of glacier-change signals. The newly identified glaciers are mostly <0.1 km². Despite their limited area, their thin ice and shorter response times may make them particularly sensitive to warming. Topographic analysis further demonstrates that supraglacial debris is preferentially distributed across low-elevation and low-slope glacier tongues, highlighting the strong controls of valley geometry, ice transport processes, and ablation-zone morphology on debris persistence. The 4 m ZY-3 DEM

https://doi.org/10.5194/egusphere-2026-2836
Preprint. Discussion started: 16 June 2026
© Author(s) 2026. CC BY 4.0 License.

highlights that high-resolution topographic information improves the delineation of glacier-units, accumulation–ablation zone structure and debris-covered tongues by preserving steep headwalls, slope discontinuities, tributary junctions, local relief and low-gradient terrain. The 2mKGI will provide a high-resolution geometric and topographic benchmark for glacier-change assessment, ice-thickness inversion, glacier-evolution modelling and next-generation automated glacier mapping in the Karakoram.

Keywords: High-resolution glacier inventory; ZY-3 DEM, Deep learning; Karakoram; Supraglacial debris

1. Introduction

Mountain glaciers are sensitive indicators of climate change and influence regional water resources, glacier-related hazards, ecosystems, and global sea level (Immerzeel et al., 2020; King et al., 2012; Kraaijenbrink et al., 2017; Sorg et al., 2012). Under ongoing glacier change, reliable inventories provide essential boundary information for quantifying glacier area and its change, estimating ice thickness and volume, reconstructing bed topography, generating flowlines, and modelling glacier evolution (Farinotti et al., 2019; Linsbauer et al., 2012; Maussion et al., 2019; Paul et al., 2017).

The Karakoram is one of the most glacierized mountain regions outside the polar regions and is characterized by extreme topographic complexity. In contrast to widespread glacier retreat in many mountain ranges, parts of the Karakoram have exhibited stable glacier extents, local advances, or near-balanced mass budgets in recent decades, a pattern commonly referred to as the “Karakoram anomaly” (Farinotti et al., 2020; Hewitt, 2005). Climate forcing alone cannot fully explain this pattern; high relief, avalanche nourishment, debris-covered tongues, large valley glaciers, and surge-type activity shape accumulation, ablation, and ice dynamics (Hewitt, 2011). These factors also hinder boundary delineation near snowlines, upper-basin margins, steep headwalls, narrow divides, and debris-covered termini, where seasonal snow, shadows, bedrock, moraines, and non-glacial debris obscure glacier extent (Paul et al., 2013). Existing inventories, including GAMDAM, SCGI, RGI, and recent Karakoram products, have improved estimates of glacier area, number, and spatiotemporal change (Guo et al., 2015; Ke et al., 2026; Mölg et al., 2018; Nuimura et al., 2015; Pfeffer et al., 2014; Xie et al., 2023). Most are based on 10–30 m optical imagery and combine spectral-index-based extraction, manual correction, topographic constraints, and increasingly machine/deep learning.

https://doi.org/10.5194/egusphere-2026-2836
Preprint. Discussion started: 16 June 2026
© Author(s) 2026. CC BY 4.0 License.

Effective regionally, these data still smooth, omit, or merge small glaciers, narrow divides, fragmented upper margins, and debris-covered tongue margins. These uncertainties propagate beyond counts and area. For debris-covered glaciers, supraglacial debris area differences can reach 30% where supraglacial debris is confused with moraines, talus, bedrock, or proglacial deposits (Paul et al., 2013). Omitting very small glaciers (<0.5 km²) can bias glacier counts and size-frequency distributions; although they account for only about 13% of glacier area and 5% of ice volume, their short response times make them important for local hydrology and near-term glacier-loss assessments (Huss and Fischer, 2016). Because glacier detection is resolution- and protocol-dependent, 10–30 m inventories may exclude small units that are resolvable in metre-scale imagery under favourable late-ablation conditions (Leigh et al., 2019). A ±10% initial-area uncertainty changes projected glacier-and-ice-cap sea-level contribution by about ±11%, while inventory choice alone can produce an 18% century-scale difference (Slangen and Van De Wal, 2011). Inventory choice can also change ice-volume estimates by 2–8% regionally and 17–25% in glacierized subregions, and may affect projected twenty-first-century mass loss more than adjacent emission scenarios (Li et al., 2023). Thus unresolved boundaries, omitted small glaciers, and generalized debris-covered margins can bias water-resource assessments, sea-level projections, and glacier-dynamic modelling.

High-resolution imagery and semantic segmentation improve automated mapping, but training-label quality, class imbalance, seasonal snow, shadows, and spectral ambiguity still limit performance (Chu et al., 2022; Xie et al., 2020; Yang et al., 2024). These limitations are particularly acute for debris-covered glaciers: surfaces resemble moraines, talus, bedrock, and proglacial deposits, while margins follow slope breaks, lateral moraines, meltwater outlets, low-gradient tongues, valley geometry, and flow-compatible terrain (Bolch, 2006; Mölg et al., 2018; Paul et al., 2004; Shukla and Ali, 2016; Xie et al., 2020; Yang et al., 2024). Reliable delineation therefore requires metre-scale optical detail and accurate topography: imagery captures texture, tone, supraglacial ponds, divides, and fragmented margins, whereas high-resolution DEMs preserve slope transitions, drainage divides, tongue morphology, and valley geometry that coarse DEMs smooth (Bolch et al., 2010; Mölg et al., 2018; Xie et al., 2023). ZY-3 tri-stereo imagery and near-synchronous DEMs provide a consistent optical-topographic basis for separating debris-covered ice from non-glacial debris and analysing Karakoram glacier morphology.

We developed 2mKGI, a high-resolution Karakoram inventory that explicitly delineates debris-covered

https://doi.org/10.5194/egusphere-2026-2836
Preprint. Discussion started: 16 June 2026
© Author(s) 2026. CC BY 4.0 License.

glaciers, using ZY-3 optical imagery, supplementary Sentinel-2 imagery, Landsat-derived land surface temperature (LST), and a 4 m ZY-3 DEM in a deep-learning and manual-refinement workflow. We aimed to produce a region-wide high-resolution inventory with quantified uncertainty; evaluate gains in small-glacier detection, debris-covered margin delineation, and glacier-unit subdivision relative to existing inventories; analyse how elevation, slope, aspect, and glacier type structure glacier area and supraglacial debris; and assess the 4 m ZY-3 DEM for interpreting morphometry, terrain transition zones, and debris-cover patterns. 2mKGI provides a high-precision geometric and topographic basis for glacier-change assessment, ice-thickness and volume estimation, evolution modelling, and automated mapping in the Karakoram.

2. Study Area and Data

2.1 Study Area

The Karakoram, located in High Mountain Asia (33.60–37.47°N, 73.72–80.50°E), is one of the most heavily glacierized mountain systems outside the polar regions (Figure 1). Elevation ranges from 1,216 to 8,519 m a.s.l. (above sea level), with a mean of 4,920 m. Approximately 28–37% of the range is glacierized, and debris-covered glaciers are especially common in the central Karakoram, where about 14.3% of glaciers contain supraglacial debris (Hewitt, 2005).

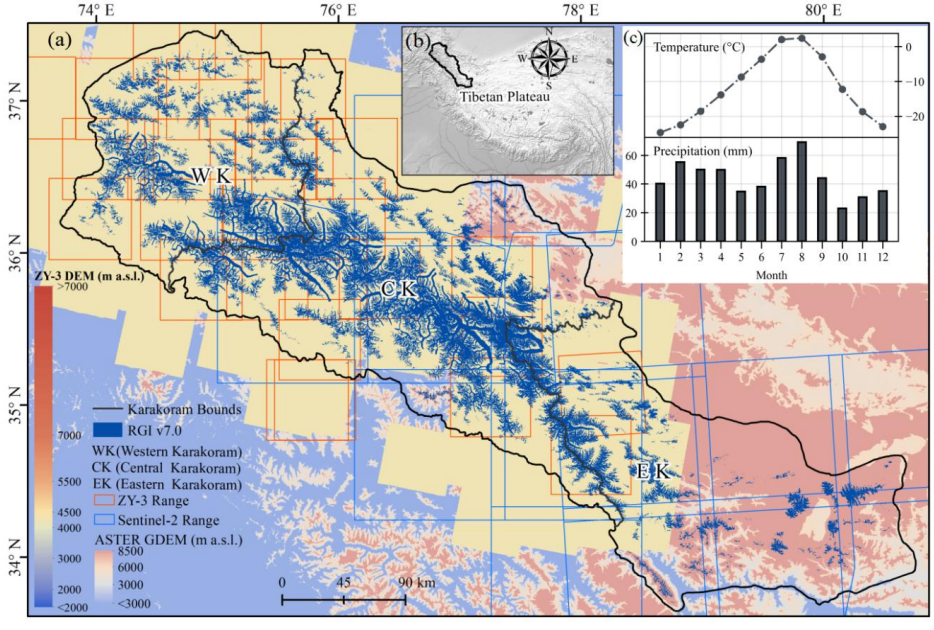

https://doi.org/10.5194/egusphere-2026-2836
Preprint. Discussion started: 16 June 2026
© Author(s) 2026. CC BY 4.0 License.

Figure 1. Study area of the Karakoram. **(a)** Glacier distribution, coverage of the ZY-3 DEM, and the ZY-3 and Sentinel-2 imagery used for boundary extraction; **(b)** geographic location of the Karakoram; and (c) mean monthly precipitation and temperature over the past two decades.

2.2 Datasets

Table 1 lists the datasets used to produce and analyse 2mKGI: ZY-3 optical/stereo imagery, Sentinel-2 multispectral data, Landsat 8 OLI/TIRS imagery, DEMs, and two reference inventories. ZY-3 supplied the primary optical data for glacier-boundary and supraglacial-debris delineation; Sentinel-2 filled gaps; Landsat 8 provided LST; and DEMs supported topographic analysis and glacier-unit subdivision.**Table 1.** Data used in this study to produce the high-resolution glacier inventory.

Data type	Data name	Resolution (m)	Application	Date	Access
Satellite imagery	Landsat 8	30 100	LST retrieval	July—October (2020, 2021)	Google Earth Engine (GEE) asset or USGS (https://earthexplorer.usgs.gov/)
	ZiYuan-3 (ZY-3)	5.8 2.1	Glacier-boundary extraction; model input	July—October (2020, 2021)	China Centre for Resources Satellite Data and Application (https://data.cresda.cn/)
		3.5	ZY-3 stereo image pair		
	Sentinel-2	10	Supplementary glacier mapping	July—October (2020, 2021)	GEE asset or ESA (https://dataspace.copernicus.eu/)
	ZY-3 DEM	4	Slope derivation; glacier-unit subdivision	2020	Generated from ZY-3 stereoscopic images
DEM	ASTER GDEM V3	30	Supplementary topographic analysis	2019	NASA (https://www.earthdata.nasa.gov/topics/land-surface/digital-elevation-terrain-model-dem.)
	SRTM (Shuttle Radar Topography Mission)	30	Regional elevation reference	2000	GEE asset or USGS (https://earthexplorer.usgs.gov/)
Glacier Inventories	KGI-2020s			2018-2020	(Xie et al., 2023) (https://doi.org/10.5194/essd-15-847-2023)
	RGI v7.0			2000	National Snow and Ice Data Center (https://nsidc.org/data/nsidc-0770/versions/7)

ZY-3 is a Chinese civilian high-resolution stereo-mapping satellite equipped with a 2.1 m nadir

https://doi.org/10.5194/egusphere-2026-2836
Preprint. Discussion started: 16 June 2026
© Author(s) 2026. CC BY 4.0 License.

panchromatic camera, a 5.8 m multispectral sensor, and forward/backward stereo cameras. We used 36 July–October ZY-3 scenes from the 2020–2021 late-ablation seasons, each with <10% cloud cover, to reduce cloud contamination and seasonal snow. The panchromatic and multispectral images supported glacier mapping, whereas the stereo images were used to generate the ZY-3 DEM. Approximately 10 Sentinel-2 images from the same late-ablation season were used to supplement areas without ZY-3 coverage, providing complete coverage of the Karakoram.

LST was derived from Landsat 8 OLI/TIRS scenes, while most topographic variables were derived from the 4 m ZY-3 DEM. ASTER GDEM V3 filled areas without ZY-3 DEM coverage, and SRTM was used as a regional reference DEM. Feature-ablation tests showed that slope and LST improved glacier mapping, particularly for debris-covered ice (Table S1). RGI v7.0 and KGI-2020s were used as comparison inventories to assess differences in glacier area, number, boundary delineation, and debris-covered glacier representation.

3. Methods

3.1 Pre-processing of satellite imagery

For each ZY-3 scene, we radiometrically calibrated, atmospherically corrected, and orthorectified the multispectral and panchromatic images, then fused the 5.8 m multispectral bands with the 2.1 m nadir panchromatic band to produce 2 m pan-sharpened multispectral images for boundary extraction. In Google Earth Engine (GEE), we processed Sentinel-2 surface reflectance from the same late-ablation windows, masked cloud and cirrus pixels, and calculated Normalized Difference Snow Index (NDSI) and Normalized Difference Water Index (NDWI) to identify clean ice, snow-covered glacier surfaces, supraglacial lakes, and adjacent water bodies. We manually checked Sentinel-2-derived outlines and harmonized them with ZY-3 outlines.

We retrieved LST from temporally matched Landsat 8 OLI/TIRS imagery in Google Earth Engine using a radiative-transfer approach. Red, near-infrared, and thermal-infrared bands were used to estimate vegetation cover, surface emissivity, and thermal radiance, from which LST was derived using the inverse Planck function (Ermida et al., 2020). All optical, thermal, and topographic layers were transformed to a common coordinate system and spatially co-registered before model training and inference. LST and slope were aligned to the 2 m ZY-3 grid for feature stacking. This enabled the model to combine high-resolution ZY-3 spectral information with thermal and topographic constraints

https://doi.org/10.5194/egusphere-2026-2836
Preprint. Discussion started: 16 June 2026
© Author(s) 2026. CC BY 4.0 License.

149 for debris-covered glacier mapping.

150 **3.2 Generation of the 4 m DEM using ZY-3 Stereo Images**

151 The Karakoram's extreme relief, steep headwalls, incised valleys, and complex glacier margins require
152 detailed topography for slope derivation, ridgeline extraction, glacier-unit subdivision, and
153 debris-covered margin interpretation. We therefore generated a 4 m DEM from ZY-3 tri-stereo imagery
154 and used it as the primary topographic dataset for glacier mapping and morphometric analysis (Figure
155 2).

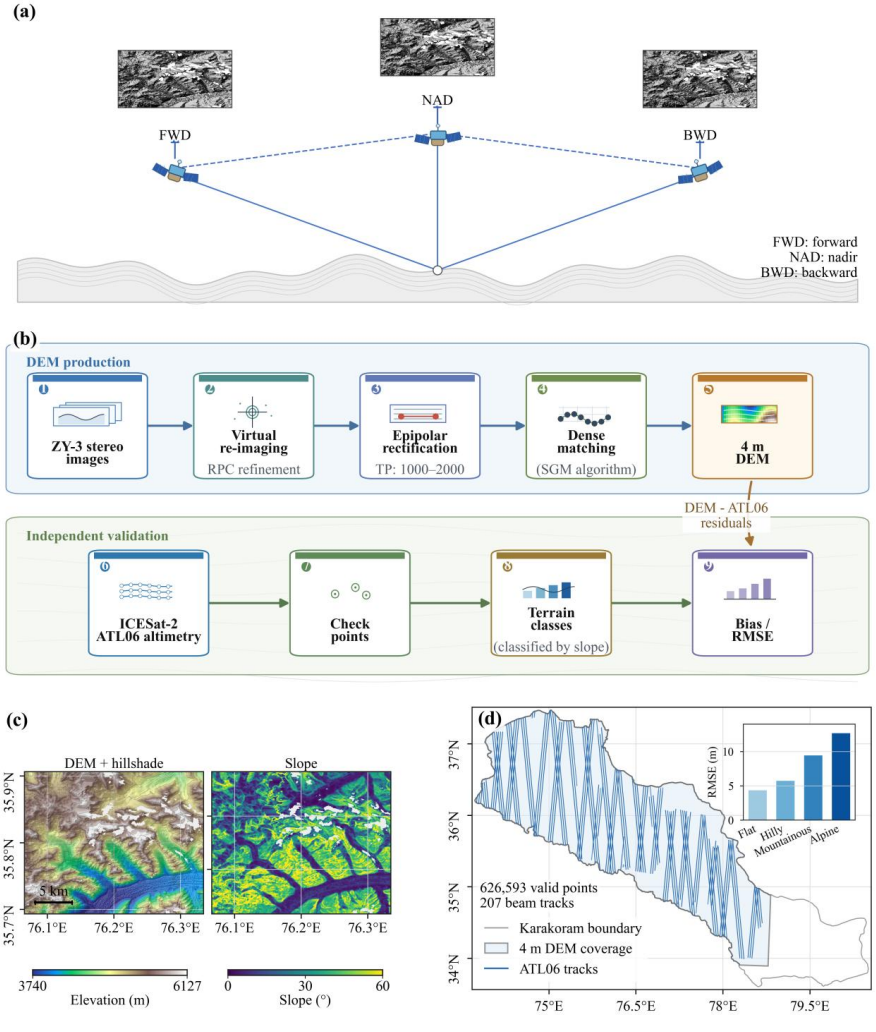

156

157 **Figure 2.** Generation and validation of the 4 m ZY-3 DEM. **(a)** Schematic diagram of ZY-3 tri-stereo

https://doi.org/10.5194/egusphere-2026-2836
Preprint. Discussion started: 16 June 2026
© Author(s) 2026. CC BY 4.0 License.

imaging geometry. **(b)** DEM production and ICESat-2-based validation workflow. **(c)** Example of the 4 m DEM and slope detail in complex glacierized terrain. **(d)** Distribution of ICESat-2 ATL06 validation tracks and RMSE values for different terrain classes in the Karakoram.

Due to the limited length of a single linear array, the ZY-3 camera's focal plane is constructed using multiple staggered CCD (Charge-Coupled Device) chips. Consequently, the raw ZY-3 stereo imagery inherently contains CCD stitching errors (which introduce interior- and exterior-orientation errors), optical distortion, sensor misalignment, and orbit/attitude uncertainties. Furthermore, it may also contain ~0.67 Hz attitude oscillations that distort image geometry (Tong et al., 2015; Wang et al., 2016; Zhang et al., 2013). Before DEM generation, we applied virtual re-imaging with an idealized virtual CCD line-array model to correct CCD stitching, array rotation and tilt, and nonlinear distortions. We also smoothed orbit and attitude observations by polynomial fitting to suppress platform jitter and attitude-oscillation effects. The corrected image-to-ground relationship is expressed in Eq. (1), where t is the imaging time of a scan line; λ is a scale factor; $\tilde{tan\psi}_x$ and $\tilde{tan\psi}_y$ represent the viewing angles of the virtual CCD in the sensor coordinate system; R_{body}^{sensor} denotes the boresight alignment matrix transforming coordinates from the satellite body frame to the sensor frame; $\tilde{R}_{ECI}^{body}$ is the rotation matrix from the Earth-Centered Inertial (ECI) frame to the satellite body frame, which is constructed from the smoothed attitude angles (i.e., roll $\tilde{\psi}(t)$, pitch $\tilde{\omega}(t)$, and yaw $\tilde{\kappa}(t)$) at time t; $R_{ECF}^{ECI}(t)$ represents the coordinate transformation matrix from the Earth-Centered, Earth-Fixed (ECF) frame to the ECI frame to compensate for the Earth's rotation; $[X,Y,Z]^T$ stands for the 3D ground coordinates of the target point in the ECF frame; and $[X_s(t),Y_s(t),Z_s(t)]^T$ is the satellite position vector in the ECF frame interpolated from the ephemeris data. This model provides a geometrically consistent basis for stereo orientation and subsequent 3D reconstruction.

$$\begin{bmatrix} \tilde{tan\psi}_x \\ \tilde{tan\psi}_y \\ 1 \end{bmatrix} = \lambda \cdot R_{body}^{sensor} \cdot \tilde{R}_{ECI}^{body}\left(\tilde{\psi}(t), \tilde{\omega}(t), \tilde{\kappa}(t)\right) \cdot R_{ECF}^{ECI}(t) \cdot \begin{bmatrix} X - X_s(t) \\ Y - Y_s(t) \\ Z - Z_s(t) \end{bmatrix} \quad (1)$$

We generated the DEM in PCI Geomatica using a rigorous sensor model adapted to ZY-3 three-line-array geometry (Deilami and Hashim, 2011). The workflow included relative and absolute orientation, epipolar resampling, dense image matching, forward intersection, interpolation, outlier removal, gap filling, and multi-scene mosaicking (Figure 2b). Relative orientation linked the forward-,

https://doi.org/10.5194/egusphere-2026-2836
Preprint. Discussion started: 16 June 2026
© Author(s) 2026. CC BY 4.0 License.

nadir-, and backward-looking images; absolute orientation transformed the stereo model into ground coordinates; and epipolar resampling reduced image matching to an approximately one-dimensional search. For each stereo pair, we automatically extracted 1,000–2,000 tie points and controlled residual vertical parallax within one pixel. Dense matching then produced conjugate points, whose 3D coordinates were calculated by least-squares forward intersection using the collinearity equations in Eq. (2). After interpolation, outlier removal, gap filling, and mosaicking, we resampled the DEM to a uniform 4 m grid for glacier-unit subdivision, slope calculation, and terrain-attribute extraction.

$$x - x_0 = -f\frac{r_{11}(X-X_s)+r_{12}(Y-Y_s)+r_{13}(Z-Z_s)}{r_{31}(X-X_s)+r_{32}(Y-Y_s)+r_{33}(Z-Z_s)}$$
$$y - y_0 = -f\frac{r_{21}(X-X_s)+r_{22}(Y-Y_s)+r_{23}(Z-Z_s)}{r_{31}(X-X_s)+r_{32}(Y-Y_s)+r_{33}(Z-Z_s)} \quad (2)$$

where (x, y) are image coordinates, (x_0, y_0) are the principal-point coordinates, f is the focal length, (X_s, Y_s, Z_s) are the sensor coordinates, r_{ij} are the elements of the rotation matrix, and (X, Y, Z) are object-space coordinates.

DEM accuracy was assessed using temporally matched ICESat-2 ATL06 laser altimetry, and the assessment was stratified by terrain category because errors in both the DEM and altimetry increase with terrain steepness (Figure 2d). The ZY-3 DEM achieved RMSEs of 4.33, 5.73, 9.44, and 12.67 m over flat, hilly, mountainous, and alpine terrain, respectively. The larger errors in alpine terrain likely reflect steep slopes, terrain shadows, surface roughness, and the sensitivity of ICESat-2 footprints to local elevation gradients. Overall, the DEM provides high-resolution topographic support for slope-constrained glacier interpretation, ridgeline-based subdivision, and analysis of glacier morphometry and supraglacial debris distribution.

3.3 Glacier-inventory workflow

3.3.1 Automated glacier mapping using multisource inputs

Glacier outlines and supraglacial debris were initially extracted using a U-Net model enhanced with the Convolutional Block Attention Module (CBAM) (Woo et al., 2018). The model used pan-sharpened ZY-3 multispectral imagery as the primary input, while Landsat-derived LST and ZY-3 DEM-derived slope were included as auxiliary channels to strengthen the thermal and topographic constraints on debris-covered glacier mapping. Training labels were manually delineated from four representative ZY-3 scenes and included three classes: background, clean ice, and debris-covered ice. Existing glacier

https://doi.org/10.5194/egusphere-2026-2836
Preprint. Discussion started: 16 June 2026
© Author(s) 2026. CC BY 4.0 License.

inventories, slope information, and Google Earth imagery were used as references during label generation. Clean-ice boundaries were mainly interpreted from spectral and textural contrast, whereas debris-covered glacier margins were constrained using slope breaks, lateral moraines, meltwater outlets, ice cliffs, and flow-compatible valley morphology. The labels were rasterized and divided into 512 × 512 pixel tiles. After data augmentation and removal of non-glacier tiles, 7,772 georeferenced samples were retained and split into training, validation, and test subsets at a ratio of 8:1:1.

During model development, we evaluated both Dice loss and Focal loss to address the severe class imbalance between supraglacial debris and background features (Figure S1). These two functions differ significantly in their optimization objectives. Focal loss is an extension of cross-entropy that introduces a modulating factor to optimize difficult pixel-level classifications; it effectively prevents the vast number of easy negatives (e.g., clear ice/snow) from overwhelming the gradient. Conversely, Dice loss is optimized for region-level similarity, directly maximizing the intersection over union between the prediction and the ground truth. While Focal loss excels at delineating hard boundaries, its pixel-wise focus can sometimes lead to fragmented predictions in complex terrain. Because Dice loss inherently prioritizes overall spatial overlap and structural integrity, it produced more continuous supraglacial-debris mappings in our experiments and was therefore adopted for the final model (Lin et al., 2017; Sudre et al., 2017). It is calculated as follows:

$$Dice\ Loss = 1 - \frac{2\sum_{i=1}^{N} p_i g_i}{\sum_{i=1}^{N} p_i + \sum_{i=1}^{N} g_i} \quad (3)$$

where p is the segmentation output generated by the model and g the actual segmentation label.

The network was trained using the Adam optimizer with a batch size of four image tiles and an initial learning rate of 1×10^{-4}, which was automatically adjusted during training. Training was run for 200 epochs, and the model converged after approximately 50 epochs (Figure S2). Dropout with a probability of 0.5 and standard data augmentation were used to reduce overfitting and improve generalization. For regional mapping, inference was performed scene by scene. Each scene was divided into overlapping 512 × 512 pixel tiles to reduce edge artefacts during mosaicking. The predicted masks were then mosaicked, vectorized, and screened to remove isolated non-glacial patches, producing the initial glacier outlines for subsequent manual refinement (Figure S3).

https://doi.org/10.5194/egusphere-2026-2836
Preprint. Discussion started: 16 June 2026
© Author(s) 2026. CC BY 4.0 License.

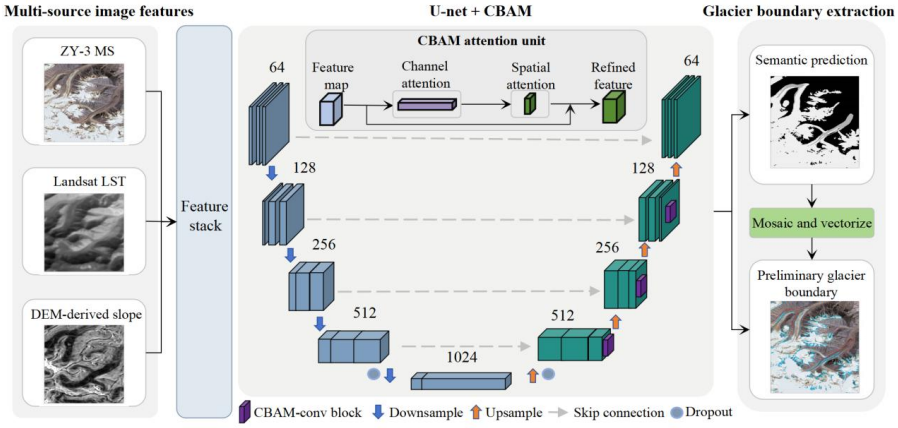

MS: multispectral imagery; LST: land surface temperature; CBAM: Convolutional Block Attention Module. Numbers denote feature channels.

Figure 3. Glacier-boundary extraction workflow based on U-Net+CBAM and ZY-3 imagery.

3.3.2 Manual refinement and glacier-unit subdivision

The automated results were manually refined to correct boundary omissions, internal holes, cloud- and shadow-related artefacts, seasonal snow contamination, and fragmented debris-covered glacier tongues (Figure 4). Manual interpretation was based on ZY-3 imagery, LST, DEM-derived slope, and Google Earth imagery. Clean-ice areas generally required only minor correction, whereas debris-covered termini and lateral margins were revised more carefully because they are spectrally similar to moraines, talus, bedrock, and proglacial deposits. Meltwater outlets, ice cliffs, slope breaks, lateral moraines, and flow-compatible valley morphology were used as key geomorphic indicators.

https://doi.org/10.5194/egusphere-2026-2836
Preprint. Discussion started: 16 June 2026
© Author(s) 2026. CC BY 4.0 License.

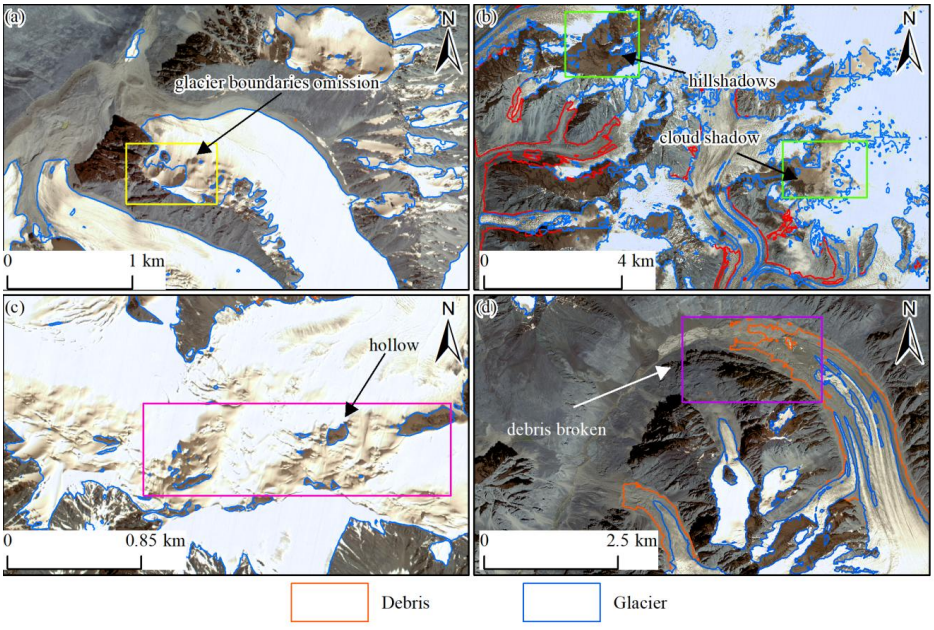

Figure 4. Typical errors in glacier outlines extracted by U-Net+CBAM from ZY-3 imagery: (a) boundary omission, (b) internal holes, (c) cloud and mountain-shadow contamination, and (d) fragmented debris mapping.

Glacier units were subdivided using DEM-derived ridgelines following drainage-basin-based methods (Bolch et al., 2010; Mölg et al., 2018; Xie et al., 2023). The 4 m ZY-3 DEM was used where available, and ASTER GDEM V3 was used elsewhere. Initial drainage divides were generated from flow-direction and basin analysis and then manually corrected using three-dimensional topographic interpretation (Figure 5). For each glacier unit, geometric and topographic attributes were extracted, including area, location, elevation, slope, aspect, DEM source, and supraglacial debris area. As summarized in Table S2, this manual revision reduced the mapped clean-ice area and increased the mapped supraglacial debris area (Table S3).

https://doi.org/10.5194/egusphere-2026-2836
Preprint. Discussion started: 16 June 2026
© Author(s) 2026. CC BY 4.0 License.

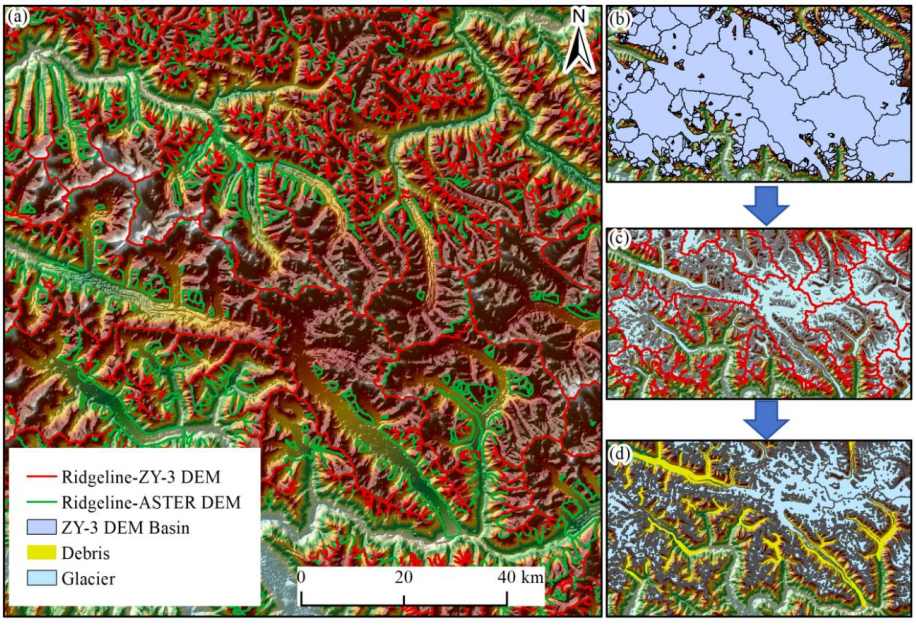

Figure 5. Ridgelines derived from the ZY-3 DEM and ASTER GDEM and used to partition glacier units. **(a)** Partial display of the ZY-3 DEM ridge lines and the ASTER DEM ridge lines, **(b)–(d)** Procedure for delineating glacial units using ZY-3 DEM ridge lines.

3.3.3 Accuracy and uncertainty assessment

The automated extraction was evaluated using an independent test dataset covering 4595.1 km² across the western, central, and eastern Karakoram. Model performance was assessed using three standard metrics derived from the confusion matrix (Deng et al., 2016; Huang et al., 2020): Overall accuracy (OA), F1 score (Chicco and Jurman, 2020; Marochov et al., 2021), Mean Intersection over Union (MIoU) (Olofsson et al., 2014). These metrics provide a robust assessment of the model's ability to delineate both glaciers and supraglacial debris. The equations are as follows:

$$\text{Accuracy} = (\text{TP} + \text{TN})/(\text{TP} + \text{TN} + \text{FP} + \text{FN}) \quad (4)$$

$$\text{F1} = \frac{2(\text{TP}/(\text{TP}+\text{FP})\times\text{TP}/(\text{TP}+\text{FN}))}{(\text{TP}/(\text{TP}+\text{FP})+\text{TP}/(\text{TP}+\text{FN}))} \quad (5)$$

$$\text{MIoU} = \frac{1}{n}\sum_{i}^{n}(\text{TP})/(\text{FN} + \text{FP} + \text{TP}) \quad (6)$$

Where TP, FP, FN, and TN represent the true positive, false positive, false negative, and true negative counts, respectively. Specifically, the F1 score provides a comprehensive evaluation by penalizing both

https://doi.org/10.5194/egusphere-2026-2836
Preprint. Discussion started: 16 June 2026
© Author(s) 2026. CC BY 4.0 License.

the over-extraction of non-target features (false positives) and the under-extraction of actual targets (false negatives). MIoU evaluates the overall spatial accuracy by calculating the average ratio of the overlapping area to the total combined area across all target classes. The model achieved an overall accuracy of 0.93 and an MIoU of 0.79. The F1 score for supraglacial debris was 0.76, with higher performance in the western Karakoram and lower performance in the eastern Karakoram, where debris cover is less extensive and spectrally similar non-glacial terrain is more common (Table 2).

Table 2. Accuracy of glacier extraction in different parts of the Karakoram.

Region	Accuracy	F1-Score (Debris)	MIoU
West	0.96	0.83	0.86
Central	0.92	0.76	0.78
East	0.92	0.65	0.72
Entire	0.93	0.76	0.79

The uncertainty of the final manually corrected inventory was estimated using both a buffer method and repeated independent digitization. A ±2-pixel buffer, equivalent to 4 m, was applied to each glacier polygon, yielding uncertainties of ±1.1% for total glacier area and ±3.8% for supraglacial debris area. In addition, a round-robin test (multi-manual Digitisation — MMD) was conducted to formally assess the boundary uncertainty of the automated extraction (Paul et al., 2013). Three independent glaciologists manually delineated 200 representative glaciers across the Karakoram via visual interpretation using ZY-3 and Google Earth imagery (Figure 6). For the statistical comparison, the arithmetic mean of the glacier areas derived from these three manual digitizations was established as the reference ground truth for each glacier. The extraction uncertainty was then quantified by calculating the relative percentage difference between our automated mapping areas and this established reference baseline. This assessment indicated an overall uncertainty of ±4.7%, with most discrepancies occurring in shadowed terrain, snow-covered areas, and debris-covered glacier margins.

https://doi.org/10.5194/egusphere-2026-2836
Preprint. Discussion started: 16 June 2026
© Author(s) 2026. CC BY 4.0 License.

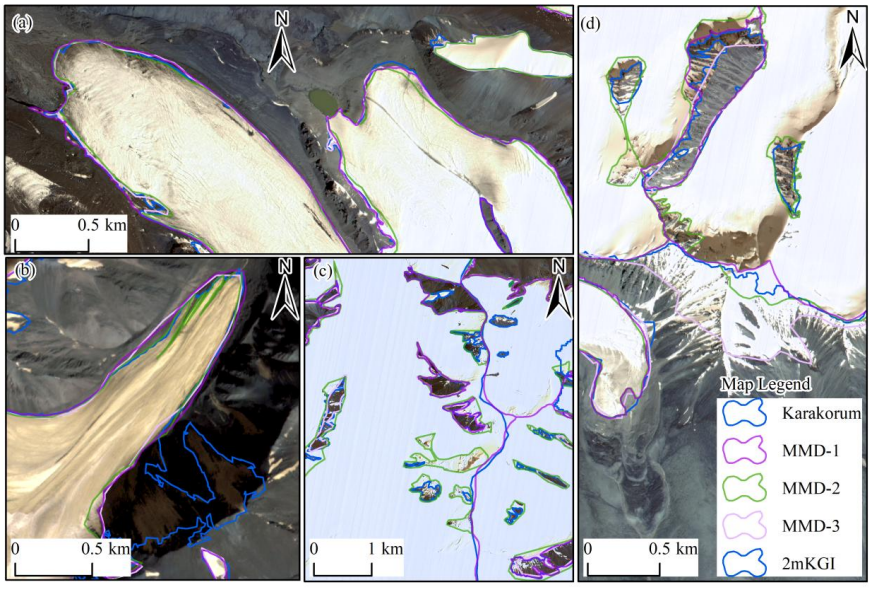

Figure 6. Glacier outlines independently digitized from ZY-3 imagery by different interpreters: **(a)** glacier termini, **(b)** mountain-shadowed areas, **(c)** perennial snowfields, and **(d)** seasonal snowfields. MMD1–MMD3 represent different digitalisation results.

4. Results

4.1 Characteristics of the Karakoram glaciers from 2mKGI

The final 2mKGI contains 13,907 glaciers larger than or equal to 0.005 km², covering a total area of 21,261.8 ± 278 km². Of this area, 19,021.9 ± 204.2 km² is clean ice and 2,239.9 ± 82.8 km² is supraglacial debris, corresponding to 10.54% of the total glacierized area. A total of 1,526 glaciers contain supraglacial debris. Approximately 21.5% of the glacier-outline coverage was derived from Sentinel-2 imagery in areas without ZY-3 coverage, whereas the remaining outlines were mapped from ZY-3 imagery. The high-resolution inventory improves glacier delineation in several settings where medium-resolution imagery commonly introduces uncertainty. The 2 m ZY-3 imagery allows glacial lakes and supraglacial ponds to be separated more clearly from glacier polygons (Figure 7a), reduces contamination from seasonal snow (Figure 7b), improves boundary interpretation in cloud- and shadow-affected terrain (Figure 7d), and provides more detailed delineation of complex glacier margins (Figure 7c). It also resolves many small glacier units in high-elevation cirques, shaded slopes, and steep tributary basins, where glacier outlines are often omitted or generalized in coarser inventories (Figure

https://doi.org/10.5194/egusphere-2026-2836
Preprint. Discussion started: 16 June 2026
© Author(s) 2026. CC BY 4.0 License.

7e).

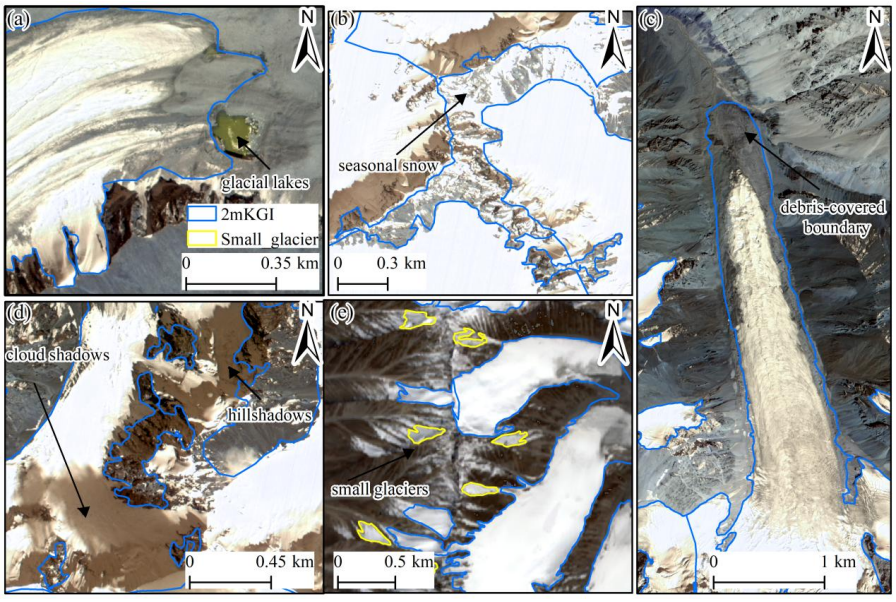

Figure 7. Advantages of high-resolution glacier mapping based on ZY-3 imagery: **(a)** exclusion of glacial lakes, **(b)** reduced interference from seasonal snow, **(c)** more precise delineation of debris-covered termini, **(d)** improved mapping in cloud- and mountain-shadowed terrain, and (e) detection of small glaciers.

Glacier number and glacier area show contrasting size-class patterns. Small glaciers dominate numerically (Figure 8b): 7,392 glaciers are smaller than 0.1 km², 3,680 glaciers range from 0.1 to 0.5 km², and 1,130 glaciers range from 0.5 to 1.0 km². In contrast, glacier area is concentrated in a small number of large glacier systems. Only 26 glaciers exceed 100 km², but together they occupy 7,406.7 km², accounting for 34.8% of the total glacierized area. This contrast indicates that the Karakoram glacier system consists of numerous very small glacier units but is areally dominated by a few extensive valley glaciers.

Spatially, glacier distribution is highly uneven across the Karakoram (Figure 8a). Glacier number is greatest in the central Karakoram, where dense glacier clusters occur around major mountain massifs and tributary basins. Glacier area is also concentrated in the central part of the range, mainly because many of the largest valley-glacier systems are located there. In contrast, the western and eastern sectors contain fewer large glacier bodies and are characterized by a higher proportion of small and medium-sized glaciers. This spatial pattern indicates that regional glacierization in the Karakoram is

https://doi.org/10.5194/egusphere-2026-2836
Preprint. Discussion started: 16 June 2026
© Author(s) 2026. CC BY 4.0 License.

333 controlled not only by the number of glacier units, but also by the presence of a few large, connected
334 valley-glacier systems.

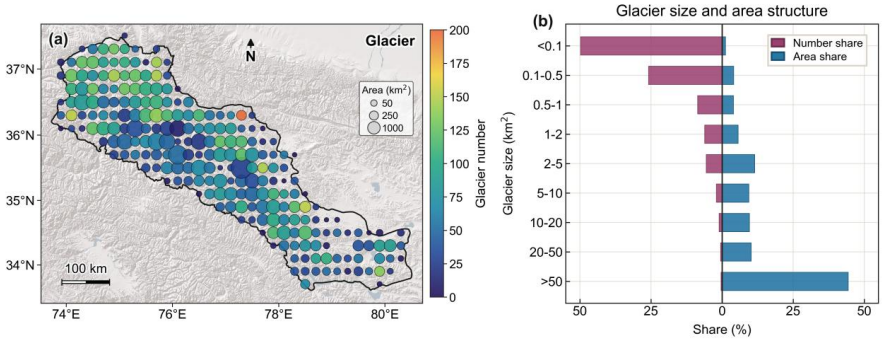

335

336 **Figure 8.** Spatial distribution and size-area structure of glaciers in the Karakoram. (a) Spatial
337 distribution of glacier number and area. Circle color indicates glacier number, and circle size indicates
338 glacier area. (b) Glacier size and area structure by area class. Left bars show number share, and right
339 bars show area share.

340 **4.2 Distribution patterns of supraglacial debris**

341 2mKGI maps 2,239.9 ± 82.8 km² of supraglacial debris, or 10.54% of the total glacierized area. Debris
342 occurs on 1,526 glaciers that together cover approximately 16,774.4 km². It is concentrated in the
343 central and western Karakoram, where large valley glaciers and long tongues dominate, but is less
344 extensive in the eastern Karakoram, where glaciers are generally smaller (Figure 9). This pattern links
345 debris distribution to glacier size, valley geometry, and low-gradient tongue development.
346 Debris-covered area is strongly concentrated on large glaciers. The 26 glaciers larger than 100 km²
347 contain 1,061.2 km² of supraglacial debris, representing 47.4% of the mapped total. Thus, nearly half of
348 Karakoram supraglacial debris lies on a small number of large valley-glacier systems, whereas
349 debris-free glaciers are generally smaller and more often occur as independent bodies in high-elevation
350 cirques, shaded slopes, or steep tributary basins.

https://doi.org/10.5194/egusphere-2026-2836
Preprint. Discussion started: 16 June 2026
© Author(s) 2026. CC BY 4.0 License.

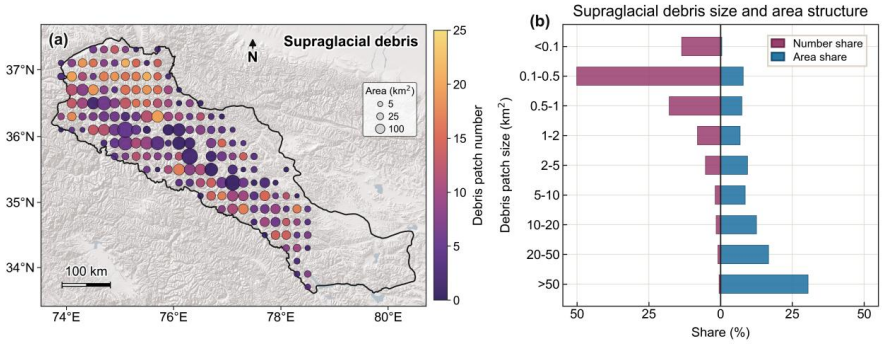

Figure 9. Spatial distribution and size-area structure of supraglacial debris in the Karakoram. **(a)** Spatial distribution of supraglacial debris. Circle color indicates debris patch number, and circle size indicates debris-covered area. **(b)** Supraglacial debris patch size and area structure by area class. Left bars show number share, and right bars show area share.

The high-resolution inventory also captures debris-covered features missed by medium-resolution products. 2mKGI identifies 247 small debris-covered glacier areas absent from KGI-2020s, with individual areas of 0.005–0.91 km². Yet its total debris-covered area is slightly smaller than KGI-2020s (2,239.9 versus 2,290 km²), showing that metre-scale mapping both recovers omitted small debris-covered units and corrects overgeneralized debris-covered termini and lateral margins.

Supraglacial debris therefore forms a spatially organized component of the Karakoram glacier system. Its concentration on large, low-gradient valley tongues may influence ablation heterogeneity, tongue persistence, and glacier response to local climate forcing. 2mKGI provides a high-resolution geometric basis for assessing how debris-covered tongues contribute to heterogeneous Karakoram glacier behaviour and the “Karakoram anomaly”.

4.3 Elevation, slope and aspect distributions

Topography strongly structures the distribution of glacier area and supraglacial debris in the Karakoram (Figure 10). Glacierized terrain spans from approximately 2400 m to more than 8000 m a.s.l., but most glacier area is concentrated in the middle- to high-elevation belt, with a clear maximum at 5600–5800 m. In contrast, supraglacial debris is mainly confined to lower elevations and peaks at 4200–4400 m. Debris-covered area declines rapidly above ~5000 m and becomes negligible above 6000 m, indicating a pronounced vertical separation between debris-covered ablation zones and clean-ice-dominated upper basins.

https://doi.org/10.5194/egusphere-2026-2836
Preprint. Discussion started: 16 June 2026
© Author(s) 2026. CC BY 4.0 License.

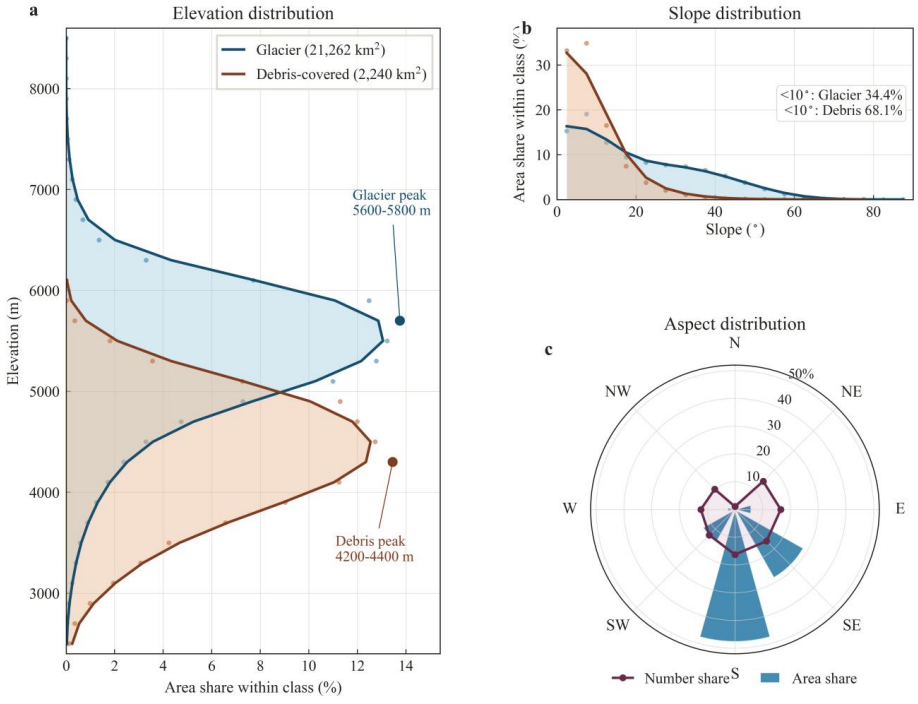

Figure 10. Topographic distributions of glacier area and supraglacial debris in the Karakoram. (a) Elevation distribution of total glacier area and supraglacial debris area. (b) Slope distribution of total glacier area and supraglacial debris area. (c) Aspect distribution of glacier number and glacier area.

Slope further differentiates clean and debris-covered glacier surfaces. Although glacier area occurs across a wide slope range, 34.4% of the total glacierized area lies on slopes below 10°. Supraglacial debris is even more strongly associated with low-gradient terrain, with 68.1% of debris-covered area occurring below 10°. Debris-covered area decreases sharply with increasing slope and is rare on slopes steeper than 30–40°. The aspect distribution shows a contrast between glacier area and glacier number. Glacier area is strongly concentrated on south- and southeast-facing slopes, which together account for 76.0% of the total glacierized area. This dominance mainly reflects the orientation of several large valley-glacier systems, whose extensive accumulation basins and tongues control the regional area signal. In contrast, glacier number is more evenly distributed among aspects because numerous small cirque, hanging, and tributary glaciers occur under more diverse local topographic conditions.

https://doi.org/10.5194/egusphere-2026-2836
Preprint. Discussion started: 16 June 2026
© Author(s) 2026. CC BY 4.0 License.

4.4 Glacier-type attributes derived from the inventory

To further examine the morphometric information contained in 2mKGI, we analysed 564 glaciers larger than 5 km² and classified them into Turkestan-, Mustagh-, and Alpine-type glaciers based on their Accumulation Area Ratio (AAR). Specifically, we utilized a published glacier albedo product (Xie et al., 2024) to approximate the snowline altitude and delineate the accumulation zone for each glacier. Following established typological criteria (Hewitt, 2011; Xie et al., 2023), the classification was executed using specific AAR thresholds: Turkestan-type ($AAR \leq 0.3$), Mustagh-type ($0.3 < AAR \leq 0.6$), and Alpine-type ($AAR > 0.6$). Finally, known surging glaciers were marked as an additional dynamic attribute (Figure 11). Alpine-type glaciers dominate the analysed sample, accounting for 51.1% of the analysed glacier area , followed by Mustagh-type glaciers with 38.7% and Turkestan-type glaciers with 10.2%. A total of 192 glaciers were identified as surging glaciers.

The glacier groups show distinct spatial patterns across the Karakoram (Figure 11). Alpine-type glaciers are widely distributed and constitute the dominant component of the analysed glacier area, particularly in the central Karakoram. Mustagh-type glaciers are concentrated mainly in the central and western Karakoram, where large valley glaciers and well-developed glacier tongues are common. Turkestan-type glaciers are less extensive and occur mainly in the southern and western parts of the region. The spatial pattern of surging glaciers broadly resembles that of Mustagh-type glaciers, suggesting that large, low-gradient valley-glacier systems in the central and western Karakoram provide favourable geometric conditions for both long glacier tongues and surge-type behaviour.

https://doi.org/10.5194/egusphere-2026-2836
Preprint. Discussion started: 16 June 2026
© Author(s) 2026. CC BY 4.0 License.

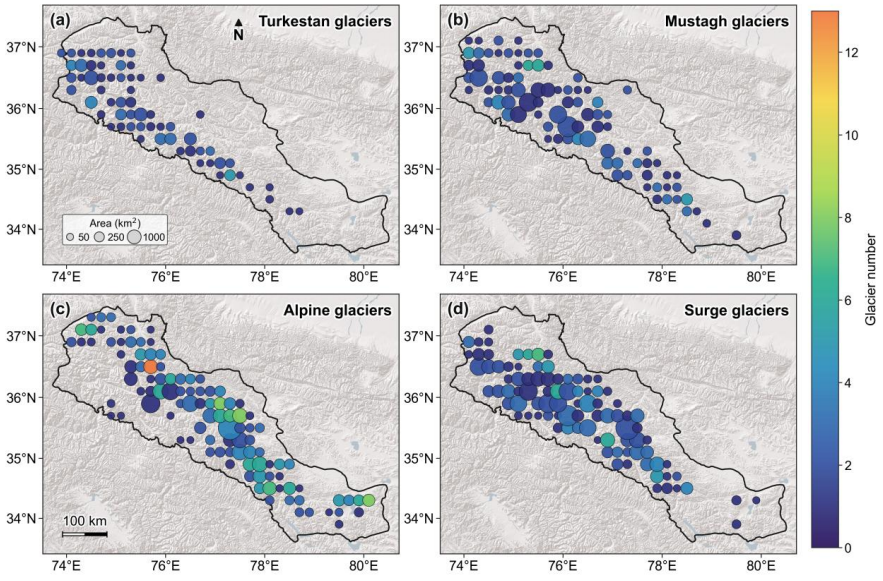

Figure 11. Spatial distribution of glacier-type attributes derived from the 2mKGI: **(a)** Turkestan, **(b)** Mustagh, **(c)** Alpine, and **(d)** surging glaciers.

The glacier types show distinct topographic settings. Alpine-type glaciers are widely distributed and occupy the highest elevations, with an area maximum at 5600–5800 m (Figure 12a). Mustagh- and Turkestan-type glaciers peak at lower elevations, mainly at 5200–5400 m and 5000–5200 m, respectively. Surging glaciers have a broader elevation distribution and are concentrated mainly between 5400 and 5800 m, indicating that surge-type behaviour is associated with large glacier systems spanning a wide altitudinal range rather than with a single elevation belt. In terms of slope, all glacier types are dominated by low-gradient surfaces, with Alpine-type glaciers showing the most extensive low-slope areas (57.4% of area below 15°), followed by Mustagh (48.3%) and Turkestan (44.3%). The steeper slope distributions of Mustagh and Turkestan glaciers are consistent with their occurrence in more rugged, high-relief terrain that favours debris accumulation and supraglacial cover, while the gentler Alpine-type profile reflects its association with broader accumulation basins and smoother valley floors (Figure 12 b, c).

https://doi.org/10.5194/egusphere-2026-2836
Preprint. Discussion started: 16 June 2026
© Author(s) 2026. CC BY 4.0 License.

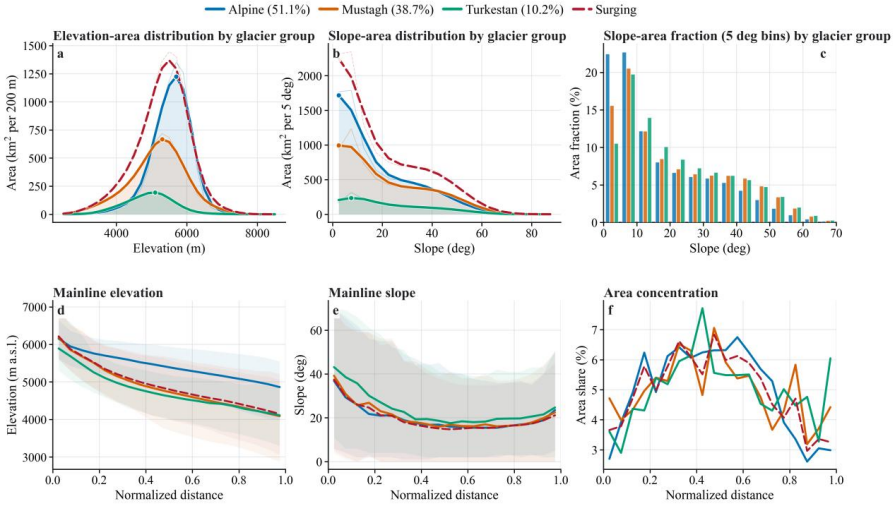

Figure 12. Topographic and longitudinal profiles of glacier types in the Karakoram. **(a)** Elevation–area distributions, **(b)** slope–area distributions, **(c)** Slope-area fraction per glacier type (5° bins), **(d)** normalized mainline elevation profiles, **(e)** normalized mainline slope profiles, and **(f)** area-concentration profiles for Alpine-, Mustagh-, Turkestan-type and surging glaciers.

Normalized mainline profiles further clarify these differences (Figure 12c–e). Alpine-type glaciers remain higher along the mainline and decline gradually from ~6100 m to ~4900 m, whereas Mustagh- and Turkestan-type glaciers descend more rapidly to lower termini of ~4100 m. Surging glaciers closely resemble the Mustagh-type profile, consistent with their association with large valley-glacier systems. In Mustagh-, Turkestan-, and surging glaciers, mainline slope decreases abruptly from steep upper basins (>35–40°) to gentler middle and lower reaches (~15–20°), with the transition concentrated at normalized distances of ~0.4–0.5. Area-concentration peaks at the same position mark the shift from narrow upper reaches to broader, low-gradient tongues. This geometry favors debris-cover development by enhancing debris supply from steep headwalls and promoting debris retention on gentler lower tongues. By contrast, Alpine-type glaciers, which are higher and more gradually graded, show less developed low-elevation debris-covered tongues.

5. Discussion

5.1 Comparison with previous glacier inventories and glaciological implications

Previous-inventory comparisons place the largest discrepancies in small glaciers and debris-covered

https://doi.org/10.5194/egusphere-2026-2836
Preprint. Discussion started: 16 June 2026
© Author(s) 2026. CC BY 4.0 License.

margins, where medium-resolution mapping is weakest (Figure 13). RGI v7.0 omits small glaciers and parts of debris-covered termini, whereas KGI-2020s generalizes debris-covered tongues and lateral margins, creating opposing biases: ice omission versus expansion of ambiguous debris-covered terrain. 2mKGI's 2 m outlines mitigate both by resolving omitted small glaciers and excluding stagnant debris, proglacial deposits, and non-glacial debris-covered surfaces. This distinction matters because debris cover modifies melt, surface lowering, ice dynamics, runoff generation, and interpretations of the Karakoram anomaly (Farinotti et al., 2020; Mölg et al., 2018; Zhu et al., 2025).

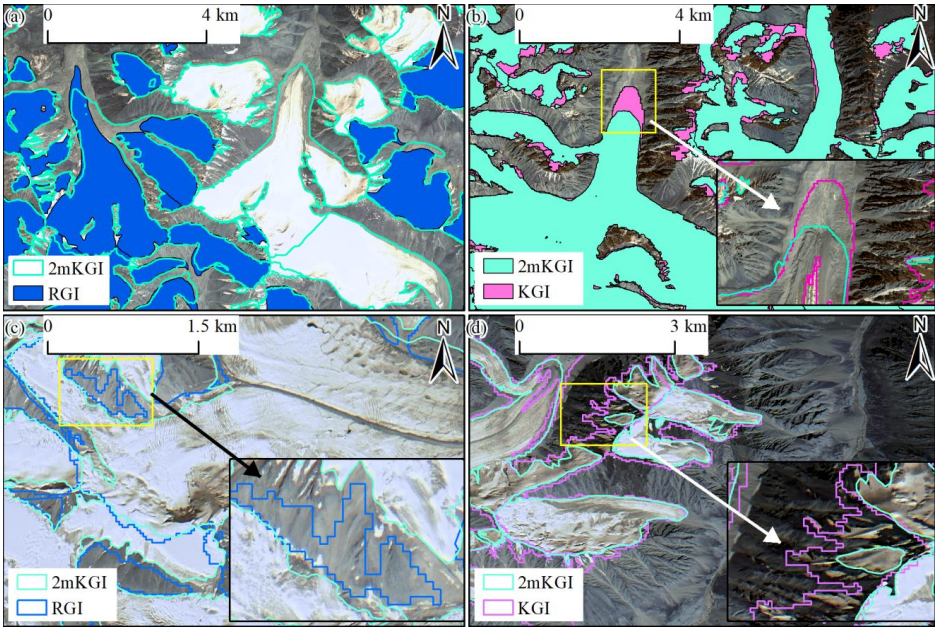

Figure 13. Comparison among glacier inventories based on ZY-3 imagery. **(a)** Comparison with RGI, highlighting glaciers omitted in RGI. **(b)** Comparison with KGI, showing differences in glacier termini and local boundary detail. **(c)** Comparison with RGI in high-altitude areas with limited glacier change. **(d)** Comparison with KGI in high-altitude terrain and glacier termini.

2mKGI chiefly revises the glacier population by adding glaciers <0.1 km². Although these glaciers contribute little to total area and probably less to regional ice volume, their limited thickness, short adjustment times, and high sensitivity to temperature and accumulation changes make them important for glacier response (Huss and Fischer, 2016). Omitting them skews assessments toward larger, slower-responding glaciers and underestimates ice bodies likely to fragment, shrink rapidly, or disappear under sustained warming. These small glaciers also reveal fine-scale climate sensitivity in the

https://doi.org/10.5194/egusphere-2026-2836
Preprint. Discussion started: 16 June 2026
© Author(s) 2026. CC BY 4.0 License.

Karakoram. Many occupy steep cirques, hanging-glacier settings, and shaded headwalls, where avalanche-fed accumulation, wind redistribution, and topographic shading can partly offset climatic forcing and reduce melt. Their responses vary: small volume and narrow elevation range make some highly vulnerable, whereas local topographic sheltering may prolong others. This supports the view that High Mountain Asia glacier change reflects climate forcing, glacier geometry, hypsometry, debris cover, and avalanche contribution (Brun et al., 2019; Farinotti et al., 2020; Sakai and Fujita, 2017).

Grid comparisons show that inventory resolution reshapes glacier-area signals (Figure S4). For RGI v7.0, we limited analysis to high-elevation accumulation areas, where real retreat should be limited and differences mainly reflect boundary uncertainty or seasonal/perennial snow inclusion. There, 2mKGI maps up to 48.41 km² less area than RGI per cell; the maximum positive difference is 15.88 km², and RGI overestimates accumulation-area extent by 607 km². For KGI-2020s, closer in acquisition period, full-region differences range from -12.9 to 7.9 km², with an overall overestimate of 1,164.2 km². These contrasts mainly reflect broader debris-covered outlines and mixed-pixel effects in the medium-resolution product.

After grid-scale uncertainty propagation, the RGI-2mKGI comparison leaves credible differences with coherent spatial structure (Figure S5): positive differences cluster in the western and north-central Karakoram, whereas negative differences are more common in the east. These inventory-based signals do not prove advance or retreat in every grid cell. Instead, they show that, where small glaciers, debris cover, and complex topography jointly affect boundaries, high-resolution inventories such as 2mKGI are essential for separating mapping artefacts from real glacier change.

5.2 Advantages of the 4 m ZY-3 DEM for glacier morphometric analysis

The 4 m ZY-3 DEM shows glacier-type-dependent resolution effects (Figure 14a–d). For Alpine-type glaciers, mean and steep-slope metrics differ most, indicating that the 30 m ASTER DEM smooths cirque walls, accumulation-zone margins, and snowline-adjacent slope breaks. Because snowfall over relatively continuous accumulation areas sustains these glaciers, such gradients are critical for interpreting accumulation-ablation partitioning and sensitivity to snowline or equilibrium-line shifts (Hewitt, 2011; Sakai and Fujita, 2017). Coarser DEMs can thus underestimate high-gradient terrain and dampen apparent climatic sensitivity. For Mustagh- and Turkestan-type glaciers, gains occur mainly in roughness and local relief. These glaciers are shaped by steep valley walls, avalanche-fed accumulation,

https://doi.org/10.5194/egusphere-2026-2836
Preprint. Discussion started: 16 June 2026
© Author(s) 2026. CC BY 4.0 License.

tributary icefalls, and complex flow routing; 4 m topography resolves short-wavelength variability around headwalls, tributary junctions, and valley-glacier transitions that 30 m data smooth. This detail matters because glacier response depends on climate forcing, snow redistribution, shading, debris supply, and low-gradient tongue geometry. The 4 m DEM therefore converts descriptive glacier-type classes into a quantitative topographic framework.

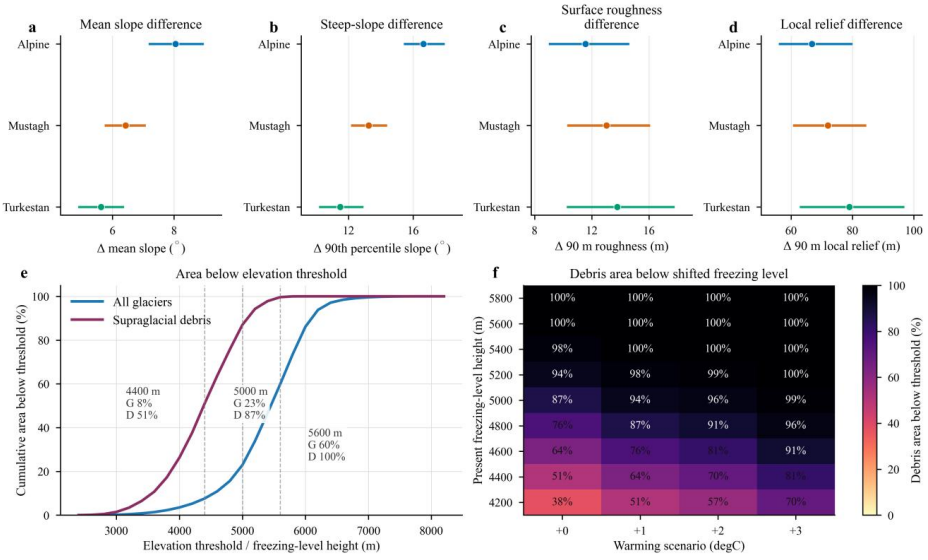

Figure 14. DEM-resolution effects and freezing-level threshold sensitivity of glacier terrain and supraglacial debris. **(a-d)** Mean differences between the 4 m and 30 m DEMs by glacier type for mean slope, 90th percentile slope, 90 m surface roughness, and 90 m local relief. Points indicate type means, and horizontal bars show 95% bootstrap confidence intervals. **(e)** Cumulative glacier area and supraglacial debris area below selected elevation thresholds. **(f)** Percentage of supraglacial debris area below the shifted freezing level under different baseline freezing-level heights and warming scenarios.

Supraglacial debris provides a second implication. Debris-covered surfaces occur lower than the overall glacierized area (Figure 14e), consistent with emergence and persistence on low-gradient ablation tongues where valley-wall input, englacial transport, flow deceleration, and sustained melt coincide. Linking debris elevation with freezing-level rise shows topographic control on climatic exposure (Figure 14f). Although distinct from the equilibrium-line altitude, the freezing level indexes thermal exposure; warming raises it, placing more debris-covered ice below freezing-level height and under positive air temperatures. In the Karakoram, where debris cover and topographic complexity

https://doi.org/10.5194/egusphere-2026-2836
Preprint. Discussion started: 16 June 2026
© Author(s) 2026. CC BY 4.0 License.

shape heterogeneous glacier behaviour and the Karakoram anomaly, this coupling is crucial (Farinotti et al., 2020; Zhu et al., 2025). Thus, the 4 m ZY-3 DEM offers not only finer terrain statistics but a process-relevant framework linking glacier type, debris distribution, and climate exposure.

5.3 Dataset value and methodological limitations

By resolving very small glaciers, narrow divides, upper-basin margins, and debris-covered termini, 2mKGI addresses two key biases in medium-resolution inventories: omission of small glaciers and overgeneralization of debris-covered margins (Mölg et al., 2018; Nuimura et al., 2015; Paul et al., 2013; Xie et al., 2023). Its clean-ice outlines, debris-covered boundaries, uncertainty estimates, and topographic attributes provide more reliable geometry for area-change assessment, hypsometric analysis, ice-thickness inversion, volume estimation, glacier-evolution modelling, and evaluation or training of automated mapping products (Farinotti et al., 2019; Linsbauer et al., 2012; Maussion et al., 2019; Paul et al., 2017). The finer glacier-unit subdivision also improves glacier-specific estimates of area, length, elevation range, slope, and hypsometry, especially in compound valley-glacier systems where coarser data poorly resolve drainage divides and tributary structures (Bolch et al., 2010; Mölg et al., 2018; Xie et al., 2023).

Limitations remain in automated high-resolution mapping. Seasonal snow, clouds, mountain shadows, supraglacial ponds, and debris-covered termini still require manual interpretation and quality control (Bolch, 2006; Paul et al., 2013; Xie et al., 2020). Directly stacking optical, thermal, and topographic variables also underuses their physical complementarity, limiting automatic separation of debris-covered ice from moraines, talus, bedrock, and proglacial deposits (Bolch, 2006; Paul et al., 2004; Xie et al., 2020). Future work should combine physically meaningful predictors, such as SAR backscatter, albedo, and surface velocity, with multimodal architectures that integrate optical, thermal, topographic, and radar constraints.

6. Conclusion

The 2mKGI provides a high-resolution glacier inventory for the Karakoram that integrates glacier outlines, supraglacial debris extent and topographic attributes. Beyond improving spatial resolution, it reveals two important biases in existing inventories: the omission of numerous small glaciers and the overgeneralization of debris-covered margins, both of which can affect assessments of glacier number, area distribution, ice volume and meltwater potential. The inventory shows that the Karakoram glacier

https://doi.org/10.5194/egusphere-2026-2836
Preprint. Discussion started: 16 June 2026
© Author(s) 2026. CC BY 4.0 License.

system is strongly scale differentiated, with small glaciers dominating in number but glacier area and supraglacial debris concentrated in a limited number of large, low-gradient valley-glacier systems. The spatial concentration of debris cover at lower elevations and on gentle tongues indicates that debris supply, valley confinement, ice transport and terrain structure jointly regulate debris accumulation and persistence. The 4 m ZY-3 DEM further improves glacier-unit subdivision and links boundary interpretation with accumulation–ablation structure, debris retention and tongue morphology. Overall, 2mKGI provides a high-resolution geometric and topographic baseline for glacier-change monitoring, ice-thickness inversion, ice-volume estimation, glacier-evolution modelling and automated glacier mapping, while future work should strengthen automated debris-covered glacier delineation through additional physical constraints and multimodal data fusion.

Data availability statement

The 2mKGI is permanently archived and freely available from the China National Cryosphere and Desert Data Centre: https://doi.org/10.12072/ncdc.glacier.db6974.2025.

CRediT authorship contribution statement

Xin Yang: Conceptualization, Methodology, Software, Formal analysis, Investigation, Data curation, Visualization, Writing – original draft. **Shiyin Liu:** Conceptualization, Supervision, Funding acquisition, Writing – review & editing. **Fuming Xie:** Data curation, Visualization, Writing – review & editing. **Jinyue Wei:** Investigation, Validation, Visualization. **Jun Zhou:** Writing – review & editing. **Yunpeng Duan:** Investigation, Validation. **Yiyuan Shen:** Investigation, Validation. **Yu Zhu:** Writing – review & editing. **Qiao Liu:** Writing – review & editing. **Muhammad Mannan Afzal:** Writing – review & editing. **Muhammad Saifullah:** Writing – review & editing.

Declaration of competing interest

The authors declare that they have no known competing financial interests or personal relationships that could have appeared to influence the work reported in this paper.

Generative AI Use Disclosure Statement

During the preparation of this manuscript, the authors used GPT-5.5 Plus for language translation, grammar checking, and improving syntactic clarity. After using this tool, the authors carefully reviewed and edited the content and take full responsibility for the final published work.

https://doi.org/10.5194/egusphere-2026-2836
Preprint. Discussion started: 16 June 2026
© Author(s) 2026. CC BY 4.0 License.

Acknowledgements

This work was supported in part by the International Cooperation and Exchange Project of the National Natural Science Foundation of China (grant no. 42361144874), the National Key Research and Development Program—Major Natural Disaster Prevention, Mitigation and Public Safety Project (grant no. 2024YFC3013402), the National Natural Science Foundation of China (grant no. 42401159), the Open Foundation of National Cryosphere Desert Data Center (Grant no. 2025NCDC013). We thank the organizations that provided the data used in this study.

References

Bolch, T.: Glacier mapping in high mountains using DEMs, Landsat and ASTER data, Grazer Schriften der Geographie und Raumforschung, 41, 13, 2006.

Bolch, T., Menounos, B., and Wheate, R.: Landsat-based inventory of glaciers in western Canada, 1985–2005, Remote sensing of Environment, 114, 127-137, 2010.

Brun, F., Wagnon, P., Berthier, E., Jomelli, V., Maharjan, S. B., Shrestha, F., and Kraaijenbrink, P. D. A.: Heterogeneous Influence of Glacier Morphology on the Mass Balance Variability in High Mountain Asia, Journal of Geophysical Research: Earth Surface, 124, 1331-1345, 2019.

Chicco, D. and Jurman, G.: The advantages of the Matthews correlation coefficient (MCC) over F1 score and accuracy in binary classification evaluation, BMC genomics, 21, 1-13, 2020.

Chu, X., Yao, X., Duan, H., Chen, C., Li, J., and Pang, W.: Glacier extraction based on high-spatial-resolution remote-sensing images using a deep-learning approach with attention mechanism, The Cryosphere, 16, 4273-4289, 2022.

Deilami, K. and Hashim, M.: Very high resolution optical satellites for DEM generation: a review, European Journal of Scientific Research, 49, 542-554, 2011.

Deng, X., Liu, Q., Deng, Y., and Mahadevan, S.: An improved method to construct basic probability assignment based on the confusion matrix for classification problem, Information Sciences, 340, 250-261, 2016.

Ermida, S. L., Soares, P., Mantas, V., Göttsche, F.-M., and Trigo, I. F.: Google earth engine open-source code for land surface temperature estimation from the landsat series, Remote Sensing, 12, 1471, 2020.

Farinotti, D., Huss, M., Fürst, J. J., Landmann, J., Machguth, H., Maussion, F., and Pandit, A.: A consensus estimate for the ice thickness distribution of all glaciers on Earth, Nature Geoscience, 12, 168-173, 2019.

Farinotti, D., Immerzeel, W. W., de Kok, R. J., Quincey, D. J., and Dehecq, A.: Manifestations and mechanisms of the Karakoram glacier Anomaly, Nature geoscience, 13, 8-16, 2020.

Guo, W., Liu, S., Xu, J., Wu, L., Shangguan, D., Yao, X., Wei, J., Bao, W., Yu, P., Liu, Q., and Jiang, Z.: The second Chinese glacier inventory: data, methods and results, Journal of Glaciology, 61, 357-372, 2015.

Hewitt, K.: Glacier change, concentration, and elevation effects in the Karakoram Himalaya, Upper Indus Basin, Mountain Research and Development, 31, 188-200, 2011.

Hewitt, K.: The Karakoram anomaly? Glacier expansion and the 'elevation effect,'Karakoram Himalaya, Mountain Research and Development, 25, 332-340, 2005.

https://doi.org/10.5194/egusphere-2026-2836
Preprint. Discussion started: 16 June 2026
© Author(s) 2026. CC BY 4.0 License.

Huang, L., Luo, J., Lin, Z., Niu, F., and Liu, L.: Using deep learning to map retrogressive thaw slumps in the Beiluhe region (Tibetan Plateau) from CubeSat images, Remote Sensing of Environment, 237, 111534, 2020.

Huss, M. and Fischer, M.: Sensitivity of very small glaciers in the Swiss Alps to future climate change, Frontiers in earth science, 4, 34, 2016.

Immerzeel, W. W., Lutz, A. F., Andrade, M., Bahl, A., Biemans, H., Bolch, T., Hyde, S., Brumby, S., Davies, B., and Elmore, A.: Importance and vulnerability of the world's water towers, Nature, 577, 364-369, 2020.

Ke, C., Xiao, Y., Fan, Y., Luo, L., Cai, Y., Shen, X., Wang, G., Wu, J., Zhuang, L., and Wang, J.: A new time-stamped glacier inventory of High Mountain Asia based on deep learning and remote sensing big data in 2020, Science China Earth Sciences, 69, 236-252, 2026.

King, M. A., Bingham, R. J., Moore, P., Whitehouse, P. L., Bentley, M. J., and Milne, G. A.: Lower satellite-gravimetry estimates of Antarctic sea-level contribution, Nature, 491, 586-589, 2012.

Kraaijenbrink, P. D., Bierkens, M. F., Lutz, A. F., and Immerzeel, W.: Impact of a global temperature rise of 1.5 degrees Celsius on Asia's glaciers, Nature, 549, 257-260, 2017.

Leigh, J., Stokes, C., Carr, R., Evans, I., Andreassen, L., and Evans, D.: Identifying and mapping very small (< 0.5 km2) mountain glaciers on coarse to high-resolution imagery, Journal of Glaciology, 65, 873-888, 2019.

Li, F., Maussion, F., Wu, G., Chen, W., Yu, Z., Li, Y., and Liu, G.: Influence of glacier inventories on ice thickness estimates and future glacier change projections in the Tian Shan range, Central Asia, Journal of Glaciology, 69, 266-280, 2023.

Lin, T.-Y., Goyal, P., Girshick, R., He, K., and Dollár, P.: Focal loss for dense object detection, 2017, 2980-2988.

Linsbauer, A., Paul, F., and Haeberli, W.: Modeling glacier thickness distribution and bed topography over entire mountain ranges with GlabTop: Application of a fast and robust approach, Journal of Geophysical Research: Earth Surface, 117, 2012.

Marochov, M., Stokes, C. R., and Carbonneau, P. E.: Image classification of marine-terminating outlet glaciers in Greenland using deep learning methods, The Cryosphere, 15, 5041-5059, 2021.

Maussion, F., Butenko, A., Champollion, N., Dusch, M., Eis, J., Fourteau, K., Gregor, P., Jarosch, A. H., Landmann, J., and Oesterle, F.: The open global glacier model (OGGM) v1. 1, Geoscientific Model Development, 12, 909-931, 2019.

Mölg, N., Bolch, T., Rastner, P., Strozzi, T., and Paul, F.: A consistent glacier inventory for Karakoram and Pamir derived from Landsat data: distribution of debris cover and mapping challenges, Earth System Science Data, 10, 1807-1827, 2018.

Nuimura, T., Sakai, A., Taniguchi, K., Nagai, H., Lamsal, D., Tsutaki, S., Kozawa, A., Hoshina, Y., Takenaka, S., Omiya, S., Tsunematsu, K., Tshering, P., and Fujita, K.: The GAMDAM glacier inventory: a quality-controlled inventory of Asian glaciers, The Cryosphere, 9, 849-864, 2015.

Olofsson, P., Foody, G. M., Herold, M., Stehman, S. V., Woodcock, C. E., and Wulder, M. A.: Good practices for estimating area and assessing accuracy of land change, Remote sensing of Environment, 148, 42-57, 2014.

Paul, F., Barrand, N. E., Baumann, S., Berthier, E., Bolch, T., Casey, K., Frey, H., Joshi, S., Konovalov, V., and Le Bris, R.: On the accuracy of glacier outlines derived from remote-sensing data, Annals of Glaciology, 54, 171-182, 2013.

https://doi.org/10.5194/egusphere-2026-2836
Preprint. Discussion started: 16 June 2026
© Author(s) 2026. CC BY 4.0 License.

Paul, F., Bolch, T., Briggs, K., Kääb, A., McMillan, M., McNabb, R., Nagler, T., Nuth, C., Rastner, P., and Strozzi, T.: Error sources and guidelines for quality assessment of glacier area, elevation change, and velocity products derived from satellite data in the Glaciers_cci project, Remote Sensing of Environment, 203, 256-275, 2017.

Paul, F., Huggel, C., and Kääb, A.: Combining satellite multispectral image data and a digital elevation model for mapping debris-covered glaciers, Remote sensing of Environment, 89, 510-518, 2004.

Pfeffer, W. T., Arendt, A. A., Bliss, A., Bolch, T., Cogley, J. G., Gardner, A. S., Hagen, J.-O., Hock, R., Kaser, G., and Kienholz, C.: The Randolph Glacier Inventory: a globally complete inventory of glaciers, Journal of glaciology, 60, 537-552, 2014.

Sakai, A. and Fujita, K.: Contrasting glacier responses to recent climate change in high-mountain Asia, Scientific reports, 7, 13717, 2017.

Shukla, A. and Ali, I.: A hierarchical knowledge-based classification for glacier terrain mapping: A case study from Kolahoi Glacier, Kashmir Himalaya, Annals of Glaciology, 57, 1-10, 2016.

Slangen, A. and Van De Wal, R.: An assessment of uncertainties in using volume-area modelling for computing the twenty-first century glacier contribution to sea-level change, The Cryosphere, 5, 673-686, 2011.

Sorg, A., Bolch, T., Stoffel, M., Solomina, O., and Beniston, M.: Climate change impacts on glaciers and runoff in Tien Shan (Central Asia), Nature Climate Change, 2, 725-731, 2012.

Sudre, C. H., Li, W., Vercauteren, T., Ourselin, S., and Jorge Cardoso, M.: Generalised dice overlap as a deep learning loss function for highly unbalanced segmentations, 2017, 240-248.

Tong, X., Li, L., Liu, S., Xu, Y., Ye, Z., Jin, Y., Wang, F., and Xie, H.: Detection and estimation of ZY-3 three-line array image distortions caused by attitude oscillation, ISPRS journal of photogrammetry and remote sensing, 101, 291-309, 2015.

Wang, M., Zhu, Y., Jin, S., Pan, J., and Zhu, Q.: Correction of ZY-3 image distortion caused by satellite jitter via virtual steady reimaging using attitude data, ISPRS Journal of Photogrammetry and Remote Sensing, 119, 108-123, 2016.

Woo, S., Park, J., Lee, J.-Y., and Kweon, I. S.: Cbam: Convolutional block attention module, 2018, 3-19.

Xie, F., Liu, S., Gao, Y., Zhu, Y., Bolch, T., Kääb, A., Duan, S., Miao, W., Kang, J., and Zhang, Y.: Interdecadal glacier inventories in the Karakoram since the 1990s, Earth System Science Data, 15, 847-867, 2023.

Xie, F., Liu, S., Zhu, Y., Qing, X., Tan, S., Gao, Y., Qi, M., Yi, Y., Ye, H., Afzal, M. M., Zhang, X., and Zhou, J.: Retrieval of high-resolution melting-season albedo and its implications for the Karakoram Anomaly, Remote Sensing of Environment, 315, 114438, 2024.

Xie, Z., Haritashya, U. K., Asari, V. K., Young, B. W., Bishop, M. P., and Kargel, J. S.: GlacierNet: A deep-learning approach for debris-covered glacier mapping, IEEE Access, 8, 83495-83510, 2020.

Yang, X., Xie, F., Liu, S., Zhu, Y., Fan, J., Zhao, H., Fu, Y., Duan, Y., Fu, R., and Guo, S.: Mapping Debris-Covered Glaciers Using High-Resolution Imagery (GF-2) and Deep Learning Algorithms, Remote Sensing, 16, 2062, 2024.

Zhang, Y., Zheng, M., Xiong, J., Lu, Y., and Xiong, X.: On-orbit geometric calibration of ZY-3 three-line array imagery with multistrip data sets, IEEE Transactions on Geoscience and Remote Sensing, 52, 224-234, 2013.

https://doi.org/10.5194/egusphere-2026-2836
Preprint. Discussion started: 16 June 2026
© Author(s) 2026. CC BY 4.0 License.

689 Zhu, Y., Liu, S.-Y., Yi, Y., Tian, L.-D., Ashraf, M., Xie, F.-M., Saifullah, M., Ali, S. H., and Grünwald,
690 R.: High-altitude precipitation controls the mass balance of Pasu Glacier, Karakoram over 2000–2020:
691 A case study based on mass and energy budget, Advances in Climate Change Research, 2025. 2025.
692